optica

Multifunctional 2.5D metastructures enabled by adjoint optimization: supplementary material

MAHDAD MANSOUREE,[1,†] HYOUNGHAN KWON,[2,†] EHSAN ARBABI,[2] ANDREW MCCLUNG,[1] ANDREI FARAON,[2] AND AMIR ARBABI[1,*]

[1]Department of Electrical and Computer Engineering, University of Massachusetts Amherst, 151 Holdsworth Way, Amherst, MA 01003, USA
[2]T. J. Watson Laboratory of Applied Physics and Kavli Nanoscience Institute, California Institute of Technology, 1200 East California Boulevard, Pasadena, CA 91125, USA
[†] These authors contributed equally.
* Corresponding author: arbabi@umass.edu

17 January 2020

This document contains supplementary methods and materials for "Multifunctional 2.5D metastructures enabled by adjoint optimization," https://doi.org/10.1364/OPTICA.374787.

Bifocal metalens: simulations and optimization. In the direct design, the responses of the nano-posts are calculated using the rigorous coupled-wave analysis technique [1]. The amplitude and transmission of the nano-posts versus nano-post width are plotted in Fig. S1.

Gradient ascent method is used to optimize the structure, using the 2.5D metasurface (designed by direct design method) as the starting point. Details about how the gradient is computed are given in the next section. For the optimization presented in Fig. 4, the step size was chosen to have an average of 2 nm absolute change in the nano-post widths in each of the first 20 iterations and 0.2 nm change in all subsequent iterations. To remove outliers (e.g., meta-atoms with large changes at the edges of the metasurface), the individual width change of each post at each was limited to 4 nm.

Electric fields were obtained by FDTD simulation [2]. The simulations shown in Fig. 4 were performed using a grid size of 33 nm. Each iteration took ~70 min on a workstation with a Xeon E7-4870 CPU and eight cores per simulation. The optimization was run for 38 iterations.

The efficiency is defined as the ratio of the power focused in a 3.6-μm-diameter aperture in the focal plane to the power incident on the metasurface. The fields immediately above the metalens were propagated to the focal plane using the plane wave expansion technique.

The structures consisted of amorphous silicon (α-Si) meta-atoms on a fused silica substrate (n=1.45) with SU-8 (n=1.58) spacer layers. The measured refractive index for the amorphous silicon varies from n=3.660 to n=3.554 over the relevant spectral range; in the simulations the average value (n=3.607) was used.

Computation of the objective function gradient. If we represent fields at the focal points of the metasurface at the two wavelengths by F_1 and F_2 (such that $I_1 = |F_1|^2$ and $I_2 = |F_2|^2$) then the partial derivative of the objective function $O = I_1 I_2 = |F_1 F_2|^2$ with respect to one of the nano-post width w_m is given by

$$\frac{\partial O}{\partial w_m} = 2I_1 \mathrm{Re}\left\{I_2 \frac{\partial F_1}{\partial w_m}\right\} + 2I_2 \mathrm{Re}\left\{I_1 \frac{\partial F_2}{\partial w_m}\right\}. \quad \text{(S1)}$$

The partial derivatives of F_1 and F_2 with respect to w_m can be computed using the adjoint technique described in Refs. [3–9], and are given by

$$\frac{\partial F_n}{\partial w_m} = j\omega_n(\epsilon_\mathrm{p} - \epsilon_\mathrm{C}) \int_{\partial\Omega_m} \mathbf{E}_\parallel^\mathrm{f} \cdot \mathbf{E}_\parallel^\mathrm{a} + \frac{1}{\epsilon_\mathrm{p}\epsilon_\mathrm{C}} D_\perp^\mathrm{f} D_\perp^\mathrm{a} \mathrm{d}s, \quad \text{(S2)}$$

where ω_n $(n = 1,2)$ is the angular frequency and ϵ_p and ϵ_C are the permittivities of the nano-post and the cladding material. The surface integral is computed over $\partial\Omega_m$ which comprises the four sides of the nano-post, $\mathbf{E}_\parallel^\mathrm{f}$ and $\mathbf{E}_\parallel^\mathrm{a}$ denote components of the forward and adjoint fields that are tangent to $\partial\Omega_m$, and $D_\perp^\mathrm{f}$ and $D_\perp^\mathrm{a}$ are the components of the forward and adjoint electric displacement fields that are normal to $\partial\Omega_m$.

Layer number and interlayer distance studies. Cylindrical lenses were employed to study the effect of layer number and spacing on device performance. For these lenses, one 100-μm-long row of posts sitting on the x-axis is repeated with 350 nm lattice constant along the y-axis. Periodic boundary conditions are imposed along the upper and lower y boundaries, and perfectly matched layers along all other boundaries. The total simulation volume is significantly smaller than that of the bifocal spherical metalens, reducing required computational resources and

enabling rapid iteration. For these studies, all nano-post widths were equal to 150 nm at the initial design step.

We first studied the effect of adding or removing layers on device efficiency by optimizing lenses with one, two and three layers. Here the summation of objective functions at individual wavelengths is used for the optimization. The results of this study are shown in Fig. S7. In each of these designs the uppermost layer consisted of 550-nm-tall amorphous silicon nano-posts clad by vacuum; lower layers in the bilayer and trilayer designs consisted of 578 nm tall amorphous silicon nano-posts clad by SU-8. Interlayer distance is the same in all designs, with a value of 500 nm. All the structures are excited by an *x*-polarized plane wave. In these optimized designs, we enabled more degrees of freedom than in the bifocal spherical metalenses: design parameters comprise meta-atom width, depth and *x* position. Figure S7 shows focusing efficiencies, here defined as the ratio of power in a 5-μm slit to the total incident power, for λ_1 = 780 nm and λ_2 = 915 nm as single-layer, bilayer and trilayer designs are optimized. Each design is optimized for approximately 80 iterations. Simulations start at 33-nm resolution with average post width change of 0.5 nm between iterations; resolution is gradually increased to 14 nm as the optimization progresses.

Next, we studied the effect of interlayer distance for bilayer cylindrical metalenses, varying the interlayer distance from 250 nm to 2000 nm. These simulations were run for close to 80 iterations with the grid size as small as 14-nm resolution. Table S2 summarizes focusing efficiencies at λ_1 and λ_2 for each of these interlayer distances, showing a relatively flat trend.

Trilayer metalens. To assess whether additional layers can improve performance, we optimized a three-layer multifunctional meta-structure using the adjoint optimization program described above. For this optimization, we selected a different design objective from the one described in the main text: the design places focal points for λ_1 = 780 nm and λ_2 = 915 nm along the *z* axis at 50 μm and 70 μm, respectively, allowing us to exploit *x* and *y* symmetries that reduce computational resource requirements. The structure, shown in Fig. S2a, consists of three design layers: The bottom two layers consist of rectangular, 580-nm-tall amorphous silicon posts clad by SU-8 which brings the height of each to 1 μm. The last layer rests on top of these, with 550-nm-tall posts clad by vacuum. The infinite half spaces above and below the design domain are made of fused silica and vacuum, respectively. Posts in each layer are located on a rectangular lattice with 350-nm pitch, and are restricted to a circular aperture with 40 μm diameter.

As discussed above, the design objective determines the excitation for adjoint simulations; in forward simulations the structure is excited by an *x*-polarized plane wave. All simulations are run at 33-nm resolution. We simulated a two-layer structure with the same design objective to allow direct comparison. The two-layer structure has an identical geometry but omits the second design layer. Instead of using conventionally-designed structures, the seed for both two- and three-layer optimizations consisted of an array of posts with uniform nano-post width $w = 140$ nm. Color-coded nano-post width maps for the three-layer structure at iteration 105, comparable to those in Fig. 4b, are shown in Fig. S2b.

Fig. S2c shows focal efficiencies (defined in the same way as described in the main text) for 780 nm and 915 nm at each design iteration. Abrupt improvements at iterations 30, 60, and 75 correspond to a reduction in the average post width change, initially 5 nm, to 2.5 nm, 1.25 nm, and 0.625 nm, respectively. The change of any individual post is limited to 100 nm at all times. After 105 iterations, the efficiency for the three-layer structure is 54% at 780 nm and 52% at 915 nm, higher than the corresponding values for the two-layer structure (40% and 32%, respectively). Longitudinal and axial intensity profiles for the three-layer structure (iteration 105) are shown in Fig. S2c.

Device fabrication. A 578-nm-thick layer of α-Si was deposited using plasma-enhanced chemical vapor deposition (PECVD) on a ~1-mm-thick fused silica substrate. For nano-patterning, we spin-coated a positive electron-beam (e-beam) resist (ZEP520A) on the sample (~300 nm). In addition, a charge-dissipating polymer (aquaSave, Mitsubishi Rayon) was spin-coated on the e-beam resist layer to avoid electrostatic charging during the e-beam lithography. The first meta-atom layer and alignment marks were patterned by an e-beam lithography system (Vistec EBPG5000+) and developed in ZED-N50 developer. A ~60-nm Al_2O_3 layer was deposited by e-beam evaporation and then the nano-pattern was transferred to the Al_2O_3 layer by a lift-off process. The Al_2O_3 layer was used as a hard mask to etch the α-Si layer in a mixture of C_4F_8 and SF_6 gases. The Al_2O_3 was then removed by a mixture of NH_4OH and H_2O_2 at 100°C.

To make a spacer between the first and second meta-atom layers, we spin-coated the SU-8 2002 at 5300 rpm and performed photo-lithography so that the alignment markers on the first layer were exposed. Subsequently, thermal reflow at 250°C was performed for the planarization of the SU-8 layer, resulting in an ~1.38 μm spacer layer. We deposited the second 550-nm thick α-Si layer and then the second layer was patterned using a procedure similar to the one used for the first layer. Finally, the removal process of Al_2O_3 is avoided because the mixture of NH_4OH and H_2O_2 could attack the SU-8 spacer layer.

Effect of misalignment between layers. Poor registration between layers can impact 2.5D metasurface performance. The device characterized in the manuscript was one of a large array of devices (ca. 700) written with deliberate shifts (up to 200 nm in both x and y directions) in an effort to produce a device with minimal misalignment between layers. Not all devices in the array were characterized. Figure S6 shows measured efficiencies for several different lateral shifts.

Measurement. A schematic of the optical setup used to measure the two focal points is shown in Fig. 5b. A 780-nm or 915-nm semiconductor laser was coupled to a single-mode fiber for illumination. The fiber was connected to a fiber polarization controller and a collimator package (Thorlabs, F220APC-850). A linear polarizer (Thorlabs, LPVIS100-MP2) was placed in front of the collimator to confirm the polarization of the input light, and the fiber polarization controller was used to maximize the power passing through the polarizer. A custom-built microscope setup, which was used to capture the focal plane intensity distributions, consists of a ×100 objective lens (Olympus, UNPlanFl) with an NA of 0.95, a tube lens with a focal length of 15 cm (Thorlabs, AC254-150-B-ML), and a CCD camera (CoolSNAP K4, Photometrics). The objective lens was mounted on the three-axis stage. To decrease the background noise, an optical longpass filter (Thorlabs, FEL0700) was placed in front of the camera. Furthermore, a flip mirror and a pinhole with a diameter of 300 μm (Thorlabs, P300D) in the image plane of the microscope were used to measure the focusing efficiency. The pinhole was mounted on the axial stage for alignment. To calculate the focusing efficiency, we divided optical power focused by the device and passed through the pinhole by the power incident on the device. The power incident on the device was measured by placing an iris instead of the pinhole and

removing the sample and adjusting the iris diameter to effectively have a 40-μm diameter at the sample plane. Moreover, the objective lens is moved along the z-axis in steps of 1 μm for obtaining the axial plane measurements shown in Figs. 5d and S4c.

References

1. V. Liu and S. Fan, "S4: A free electromagnetic solver for layered periodic structures," Comput. Phys. Commun. **183**, 2233–2244 (2012).
2. A. F. Oskooi, D. Roundy, M. Ibanescu, P. Bermel, J. D. Joannopoulos, and S. G. Johnson, "MEEP: a flexible free-software package for electromagnetic simulations by the FDTD method," Comput. Phys. Commun. **181**, 687–702 (2010).
3. M. Mansouree and A. Arbabi, "Large-scale metasurface design using the adjoint sensitivity technique," in *Conference on Lasers and Electro-Optics (CLEO)* (2018), p. FF1F.7.
4. M. Mansouree and A. Arbabi, "Multi-layer multifunctional metasurface design using the adjoint sensitivity technique," in *High Contrast Metastructures VIII* (SPIE, 2019), p. 59.
5. M. Mansouree and A. Arbabi, "Metasurface design using level-set and gradient descent optimization techniques," in *International Applied Computational Electromagnetics Society Symposium* (2019).
6. O. D. Miller, "Photonic design: from fundamental solar cell physics to computational inverse design," University of California, Berkeley (2012).
7. H. Chung and O. D. Miller, "High-NA achromatic metalenses by inverse design," arXiv:1905.09213 (2019).
8. D. Sell, J. Yang, S. Doshay, R. Yang, and J. A. Fan, "Large-angle, multifunctional metagratings based on freeform multimode geometries," Nano Lett. **17**, 3752–3757 (2017).
9. T. Phan, D. Sell, J. Yang, S. Doshay, and J. A. Fan, "Metasurface lenses based on topology-optimized wavelength-scale building blocks," in *Conference on Lasers and Electro-Optics (CLEO)* (2018), p. FF3C.6.

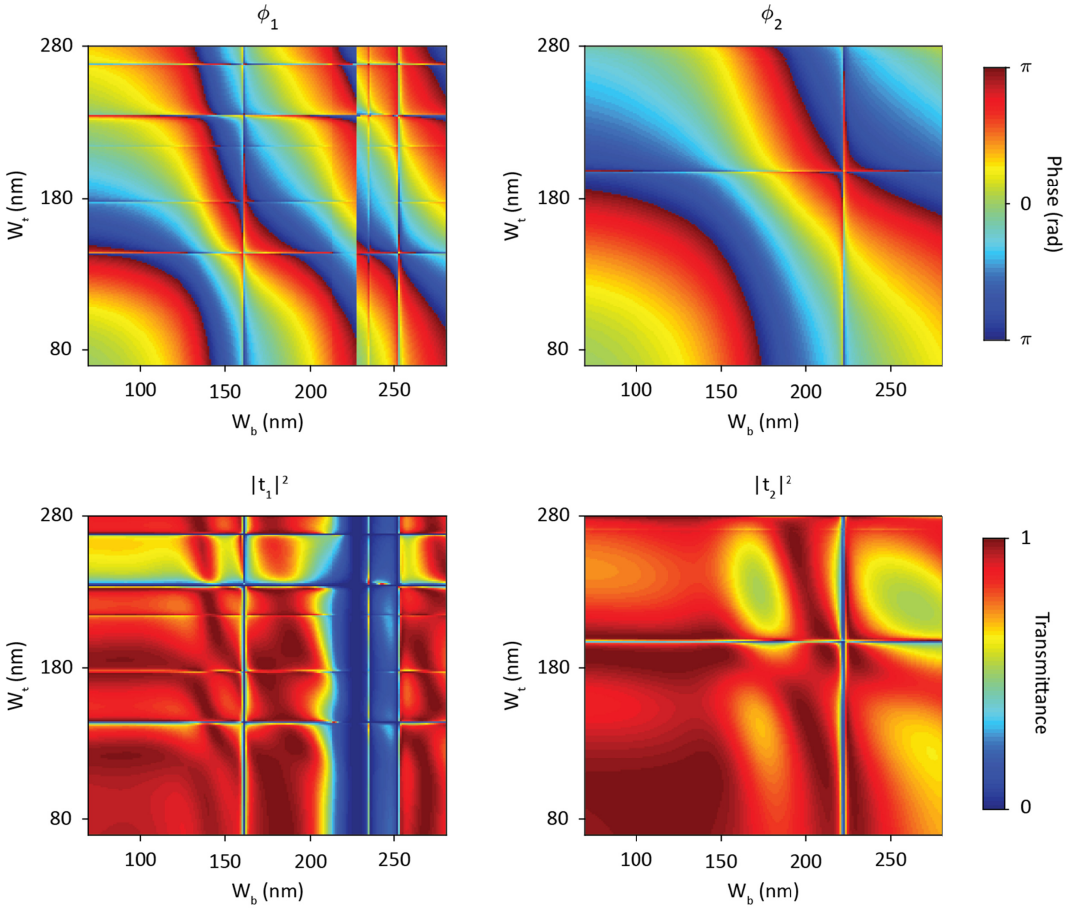

Figure S1. Simulated transmittances and the phases of the transmission coefficients at 780 nm and 915 nm for the periodic bilayer metastructure shown in Fig. 2a as functions of the bottom and top nano-post widths.

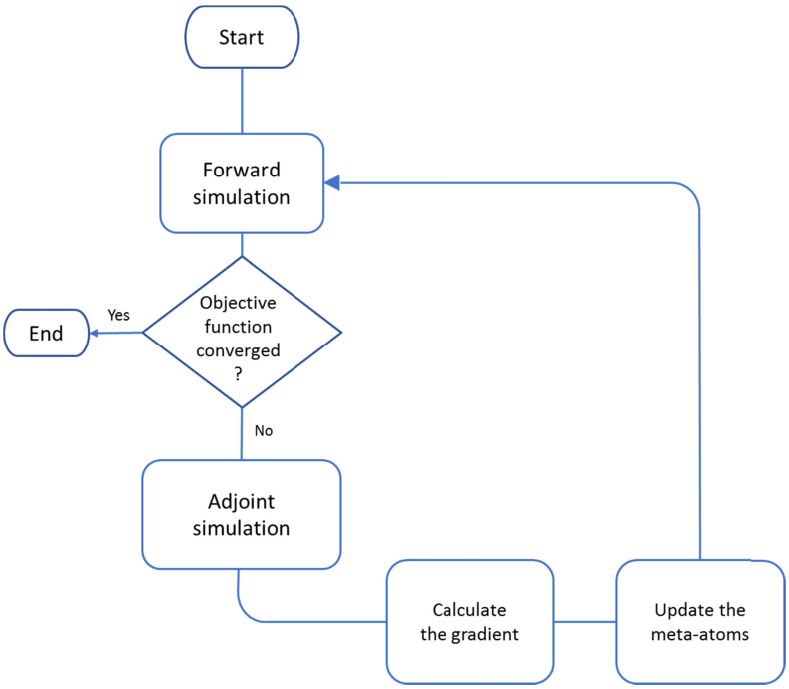

Figure S2. Optimization flowchart. Forward and adjoint simulations are performed and the gradient vector is calculated. Meta-atom widths are updated using the gradient information. This process is iterated until the objective function is converged.

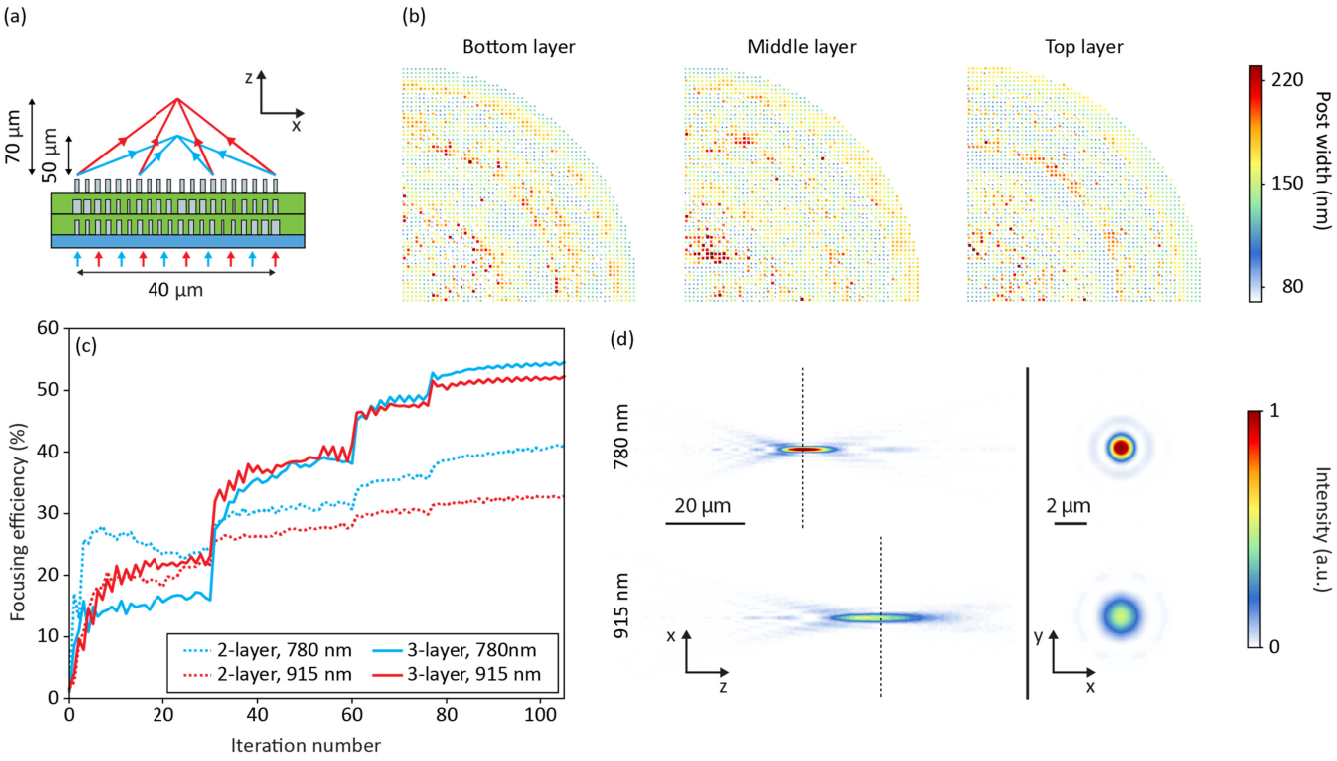

Figure S3. (a) Schematic of trilayer metalens. (b) Color-coded plots of the nano-post widths in the bottom, middle and top layers for the trilayer metalens at iteration 105. Because the structure has *x* and *y* mirror symmetries only one quadrant is shown. (c) Evolution of the focusing efficiencies for two- and three-layer lenses at each design wavelength as optimization progresses. (d) Longitudinal (left) and axial (right) intensity profiles for the trilayer metalens at iteration 105. Black dashed lines indicate focal planes at 50 µm and 70 µm.

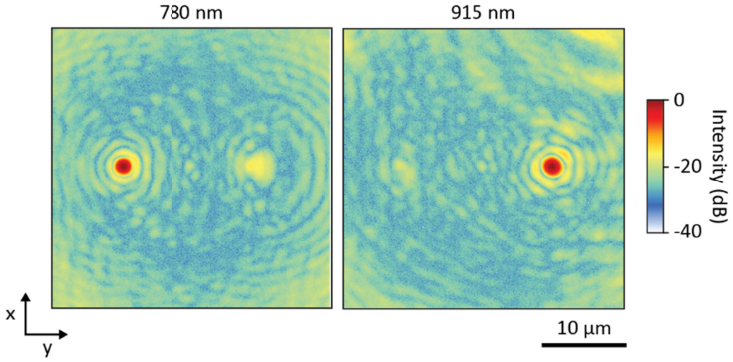

Figure S4. Measured focal plane intensity distributions of the optimized metalens on a logarithmic-scale at 780 nm and 915 nm.

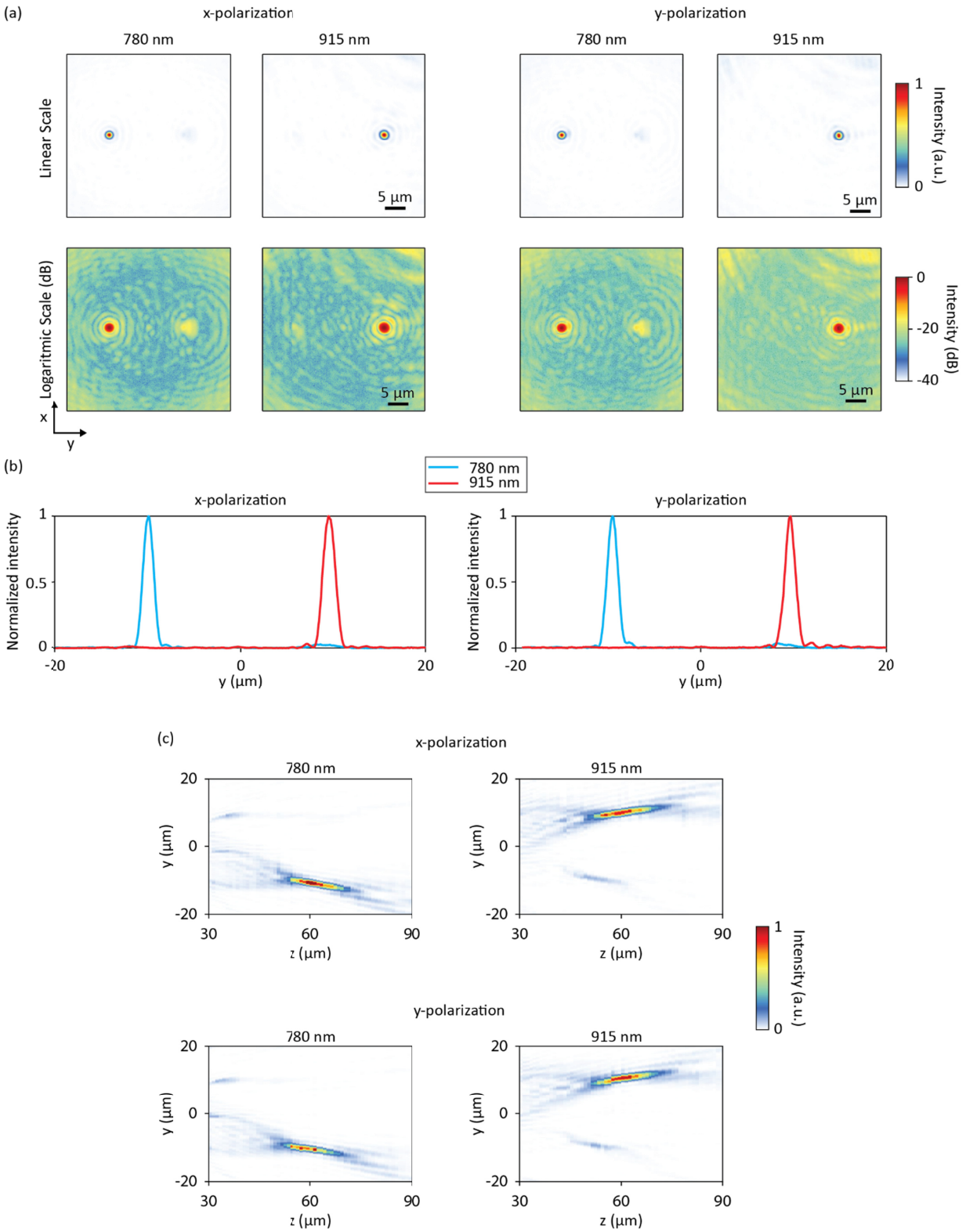

Figure S5. Polarization-resolved measurements of the optimized metalens. (a) Measured focal plane intensity distributions for *x*- and y-polarized incident light on linear and logarithmic scales. (b) Focal plane intensity profiles along the *x*=0 line for *x*- and y-polarized incident light. (c) Measured intensity distributions in the *y*-*z* plane for *x*- and *y*-polarized incident light.

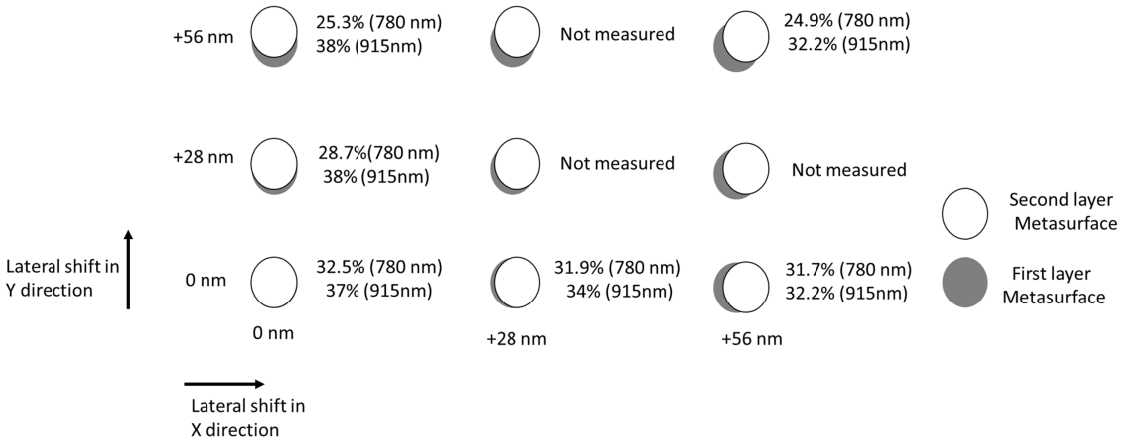

Figure S6. Schematic diagram of measured efficiencies for different inter-layer shifts. Values for the 2.5D metasurface described in the main text are shown in the lower left corner.

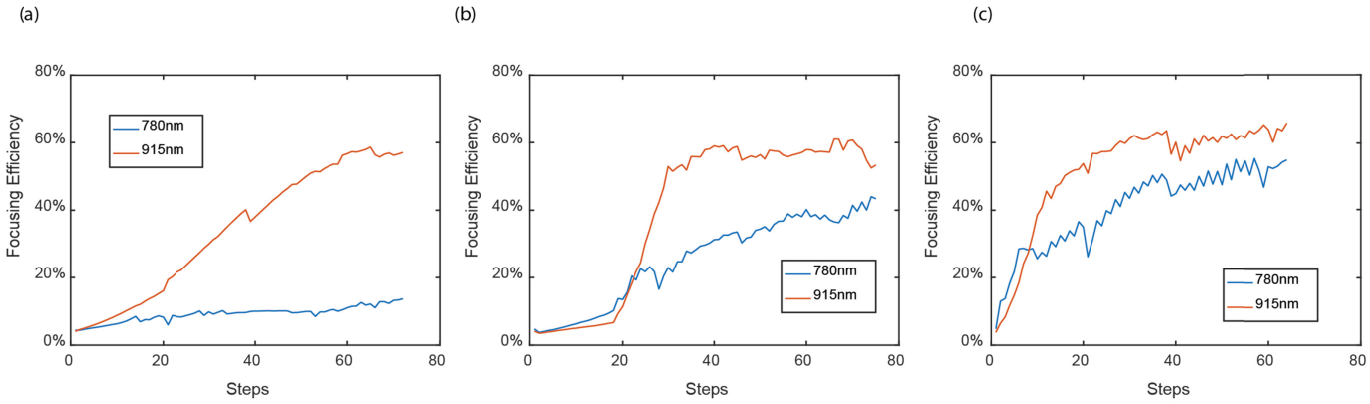

Figure S7. Progress of the optimized cylindrical lenses with different number of layers. Efficiency values (a) for monolayer, (b) bilayer, and (c) trilayer lens. The focusing efficiency is defined as the percentage of the incident power that is focused into a 5-μm-wide slit in the focal plane of the lens.

Interlayer distance	Effciency at 780 nm	Efficiency at 850 nm	Average efficiency
250 nm	30.09	66.23	48.16
500 nm	43.32	53.32	48.32
750 nm	42.12	60.13	51.13
1000 nm	39.90	61.76	50.83
1250 nm	41.58	57.71	49.65
1500 nm	44.46	54.90	49.68
1750 nm	48.19	55.56	51.88
2000 nm	44.43	59.05	51.74

Table S1. Focusing efficiency values for bilayer metasurfaces with different interlayer distances at the two design wavelengths.